Froth surface shape measurement using non-invasive photogrammetric methods

Tine Marquardt[a,b,*], Tobias Lappan[a,b], Kerstin Eckert[a,b], Sascha Heitkam[a,b]

[a] *Institute of Fluid Dynamics, Helmholtz-Zentrum Dresden-Rossendorf, Dresden, Germany*
[b] *Institute of Process Engineering and Environmental Technology, Technische Universität Dresden, Dresden, Germany*

Abstract

Froth monitoring has great potential for optimizing flotation processes as the froth phase strongly influences the overall flotation performance. The overflowing froth height is commonly used to estimate the air recovery, and typically measured point-wise using laser distance sensors based on a time-of-flight principle. We present stereo photogrammetry as a non-invasive, triangulation-based technique for determining the froth surface shape. This allows to analyze the froth height across a larger area. The technique has been tested in a laboratory-scale flotation experiment, demonstrating relations between the froth height profile and local froth flux. Additionally, it allows a simultaneous measurement of bubble sizes and froth stability. Overall, measuring the froth surface shape across an area provides a more accurate basis for estimating the air recovery and offers valuable insights into froth rheology, highlighting the potential for enhanced froth monitoring and process control in industrial-scale, continuously operated flotation cells.

Keywords: Froth flotation, Froth height, Froth stability, Image processing

1. Introduction

The froth zone plays a crucial role in the recovery of valuable minerals by froth flotation. Understanding phenomena such as froth transport, mobility and stability is essential for optimizing flotation processes and scaling up industrial flotation cells (Mesa and Brito-Parada, 2019). Flotation plant froth zone monitoring relies strongly on optical observations and imaging-based measurement techniques, as they allow contactless and real-time measurement of froth properties. Froth measurement systems typically extract physical features such as bubble size, shape, color, froth velocity, and stability from two-dimensional (2D) froth images using established image processing techniques including various segmentation algorithms (Aldrich et al., 2010). More advanced analyses incorporate statistical methods such as Fourier transforms (Aldrich et al., 2010). Moreover, machine learning algorithms are becoming increasingly important for froth analysis (Aldrich et al., 2022).

However, these 2D approaches are limited, as they are missing information on the height and three-dimensional (3D) surface shape of the froth, which are essential for characterizing its mobility and stability more comprehensively. Therefore, recent studies have increasingly focused on using imaging-based techniques for reconstructing the 3D

*Corresponding author
Email address: t.marquardt@hzdr.de (Tine Marquardt)

froth surface over larger areas. For instance, Zhao et al. (2019) proposed a method for 3D froth reconstruction using a single camera based on defocus blur and illumination of the froth bubbles. Hu et al. (2024) used a deep learning-based approach with stereo imaging by two cameras to achieve three-dimensional froth reconstruction. Zhong et al. (2024) measured froth depth using a binocular camera system by employing the white reflection points on the top of bubbles. Likewise, Zheng et al. (2024) used binocular cameras to predict froth depth via stereo disparity and deep learning. Additionally, Luo et al. (2023) proposed a specialized calibration method for binocular imaging systems in froth flotation cells.

Stereo photogrammetry is a well-established image processing technique for various engineering applications such as deformation analysis, materials testing, or production control (Luhmann et al., 2020). It offers a promising approach for improving the accuracy and spatial resolution of froth measurements by reconstructing the full 3D froth surface from two or more 2D images. By detecting and matching corresponding image features in time-synchronized, overlapping image pairs, and applying triangulation using known camera parameters, it generates dense 3D point clouds that represent the froth surface topology. The obtained 3D froth features enable a more detailed and spatially resolved analysis of flotation phenomena such as the froth transport, stability and mobility at the flotation cell lip. Besides froth characterization, the 3D measurement also improves the accuracy of froth performance indicators such as air recovery (Hadler and Cilliers, 2009) by providing spatially resolved measurements of froth height and surface velocity.

Our previous experimental works have focused on measuring the height of froth or two-phase gas-liquid foam in various experimental setups using different measurement techniques. This includes the optical measurement of the froth height and depth in a laboratory-scale batch flotation cell through its transparent side wall (Marquardt et al., 2025a), the evaluation of laser-based techniques, namely a lidar sensor and an industrial laser line scanner, for foam and froth height measurement (Marquardt et al., 2024), and the characterization of height profiles of overflowing foam by means of this line scanner (Marquardt et al., 2025b). In terms of the measurement area, these techniques are limited: they provide the height data averaged in a rather small, point-like area or along a line at the foam or froth surface.

In this work, we present a 3D imaging method for reconstructing froth surfaces using stereo photogrammetry with two calibrated cameras and image disparities. The method is demonstrated on a laboratory-scale flotation cell with overflowing froth. From the resulting 3D froth surface shape, spatially resolved height profiles at the cell lip are extracted. Examples illustrate the analysis of the froth flow using these height profiles, demonstrating the ability of the proposed approach to analyze mobility and stability characteristics of flotation froth.

2. Methods

To demonstrate stereo photogrammetric surface reconstruction for froth flotation, a laboratory-scale bottom-driven Magotteaux flotation cell was used. This setup provides free optical access to the froth surface for two grayscale

cameras. The setup is sketched in Figure 1a.

2.1. 3D froth surface reconstruction method

Stereo photogrammetry is used to reconstruct the 3D shape of the froth surface in the object coordinate system (X, Y, Z) from a pair of 2D images acquired from a flotation cell (image coordinate systems $(x_1, y_1), (x_2, y_2)$) by means of image rectification and calculation of disparities. The steps of the froth surface reconstruction method are illustrated in Figure 1.

For image acquisition, two time-synchronized cameras are positioned perpendicular to the froth surface, as shown in Figure 1a. A calibration, e.g. using a checkerboard pattern, is performed to determine the intrinsic parameters of both cameras and their relative position (Figure 1b). Additionally, the position of the cameras in the object coordinate system is obtained by marking a set of reference points of known position on the edge of the flotation cell. Using the calibrated camera parameters, the images are rectified to correct for the lens distortion and relative position of the two cameras (Figure 1c). This process projects the images onto a common image plane, aligning the epipolar lines horizontally, as if the cameras were perfectly parallel. The resulting reprojection matrix $\mathbf{Q}$ will be used in a later step to transform coordinates into the object coordinate system of the flotation cell. The matrix contains the focal length f and the principal point $[c_x, c_y]$ of the rectified camera 1, and the baseline, or distance, b between the virtual rectified camera centers

$$\mathbf{Q} = \begin{bmatrix} 1 & 0 & 0 & -cx \\ 0 & 1 & 0 & -cy \\ 0 & 0 & 0 & f \\ 0 & 0 & 1/b & 0 \end{bmatrix}. \tag{1}$$

After rectification, corresponding points lie on the same row, i.e. at identical y-coordinates, in the images recorded by the cameras 1 and 2. This improves both the efficiency and accuracy of the following estimation of disparities by significantly reducing the search space for corresponding points. The disparity p_x is defined as the difference in horizontal coordinates (x-coordinates) between corresponding points in the rectified image pair

$$p_x = x_{1,\,\text{rect.}} - x_{2,\,\text{rect.}}. \tag{2}$$

The disparity is inversely proportional to the depth of the point relative to the camera plane. The resulting disparity map shown in Figure 1d represents the horizontal displacement between all corresponding pixels in the image pair. Here, the disparity map is computed using semi-global matching (Hirschmüller, 2005; The MathWorks, Inc., 2025a). This method generates accurate and smooth disparity maps covering the majority of pixels in the froth image due to robust handling of repetitive patterns and image noise. The disparity can be computed only in the area where the two camera images overlap. Pixels that lie outside this common field of view are marked in gray in Figure 1d.

Using the disparity map and the stereo reprojection matrix $\mathbf{Q}$, the 3D homogeneous coordinates $(\tilde{X}_c, \tilde{Y}_c, \tilde{Z}_c)$ of the

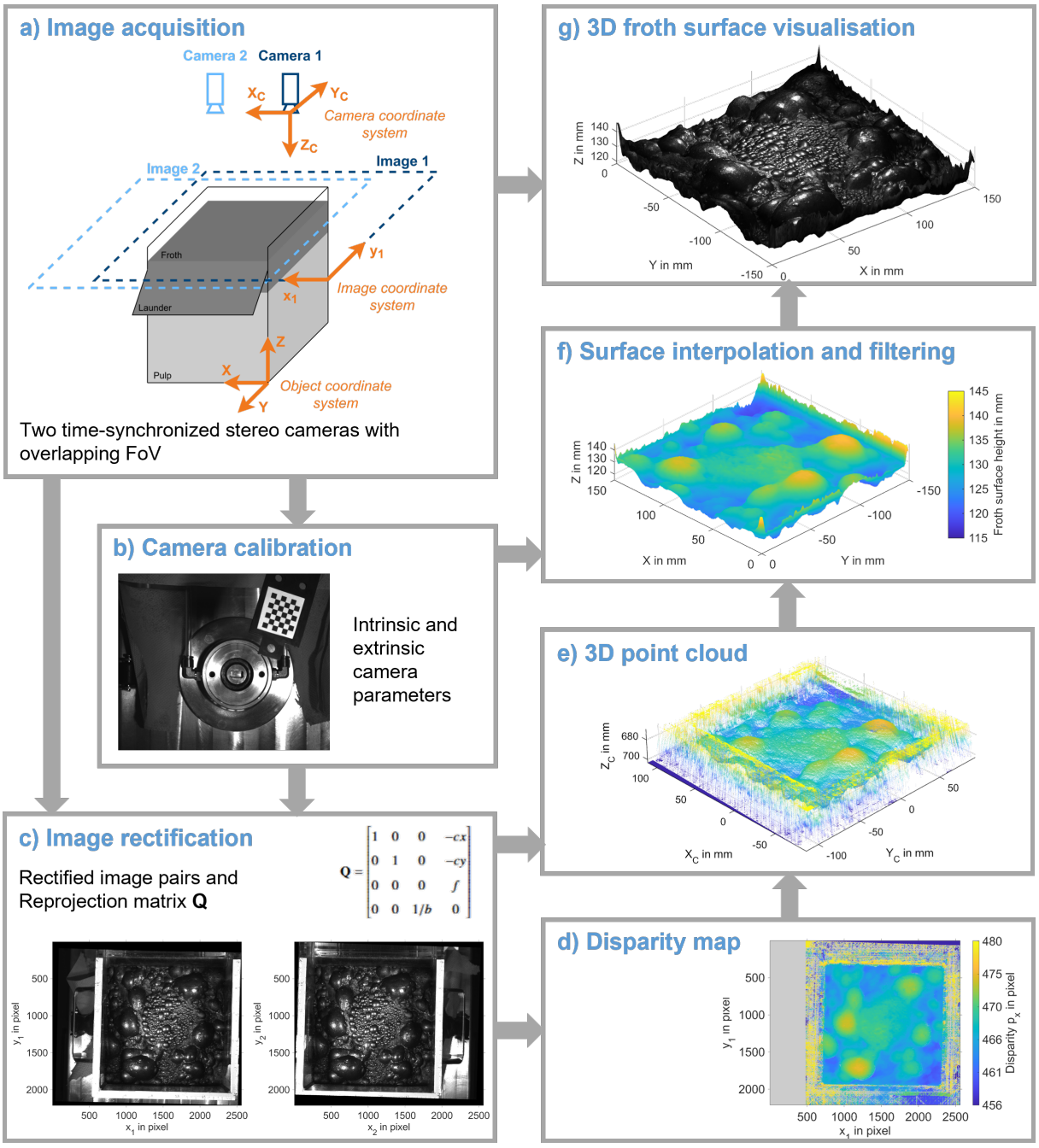

Figure 1: Workflow for 3D surface reconstruction of flotation froth using stereo photogrammetry. The method is demonstrated for a non-overflowing froth in a laboratory flotation cell.

scene are reconstructed. These are then converted to Euclidean coordinates (X_c, Y_c, Z_c) in the coordinate system of

camera 1 using the homogeneous coordinate W, which serves as a scaling factor

$$\begin{bmatrix} \tilde{X}_c \\ \tilde{Y}_c \\ \tilde{Z}_c \\ W \end{bmatrix} = \mathbf{Q} \cdot \begin{bmatrix} x \\ y \\ p_x \\ 1 \end{bmatrix}, \quad (X_c, Y_c, Z_c) = \left(\frac{\tilde{X}_c}{W}, \frac{\tilde{Y}_c}{W}, \frac{\tilde{Z}_c}{W} \right). \tag{3}$$

The resulting point cloud is shown in Figure 1e. For subsequent data analysis, the point cloud is transformed to the object coordinate system of the flotation cell using the calibration data (Figure 1f). Points outside the geometrically valid range defined by the experimental setup are removed from the point cloud. Errors in depth estimation result from an incorrect matching of homologous points and, hence, over- or underestimated disparities. Additionally, disparity values cannot be determined for some pixels in textureless regions or because of strong local reflections in the froth images. These image pixels are marked in gray in Figure 1d.

Afterwards, the points are interpolated onto a regular grid using a natural neighbor interpolation (The MathWorks, Inc., 2025b). The reconstructed surface is smoothed using a Gaussian filter to reduce noise and improve surface smoothness and continuity. The result is shown in Figure 1f. This 3D reconstruction can then be used to visualise the froth surface shape (Figure 1g) and to analyse various froth properties.

2.2. Experimental setup and image acquisition

The 3D froth surface reconstruction method was demonstrated using overflowing froth in a laboratory-scale flotation cell. Experiments were conducted in a 2.5 L Magotteaux cell with a cross-sectional area of 15 cm × 15 cm. In this mechanical flotation cell, air is introduced through a rotor at the bottom of the cell, enabling free optical access from the top. A binary particle system consisting of 10 % magnetite and 90 % quartz was used, with sodium oleate (0.027 g L^{-1}) as collecter and MIBC (methyl isobutyl carbinol, 0.0045 g L^{-1}) as frother. These surfactants were added sequentially, followed by 2 min of conditioning each. After conditioning, the rotor speed was set to 800 rpm and the air flow was initiated at a rate of 5 L min^{-1}. The resulting gas holdup and simultaneous formation of a froth layer after turning the air on caused the pulp-froth interface to rise in the flotation cell, leading to an overflow of froth into the launder for approximately 20 s. This duration is sufficient to demonstrate the applicability of the photogrammetric method to overflowing flotation froth. For future studies, a continuously operated flotation cell would enable longer measurement periods.

The overflowing froth was captured by two grayscale CMOS cameras (JAI GO-5100M), each acquiring images of size 2464 pixel × 1028 pixel. To achieve a large overlapping field of view, the cameras were mounted approximately 69 cm above the froth, oriented to be parallel with approximately 4.5 cm lateral distance and perpendicular to the froth surface. Minor geometric deviations were fully corrected via calibration. The overlapping image area of 70 % covered the full width of the front section of the flotation cell and the launder. The two cameras were time-synchronized by a hardware trigger and operated at a frame rate of 50 frames per second. Stereo calibration was performed using 128

image pairs of a 6-by-7 checkerboard pattern, yielding the intrinsic and extrinsic parameters of both cameras. A mean reprojection error of 0.27 pixel was achieved, indicating high calibration accuracy. The froth surface height at each pixel was computed using stereo photogrammetry and interpolated onto a regular grid with a resolution of 10 points mm^{-1}. This 3D reconstruction serves as the basis for subsequent analysis of the froth surface.

3. Results

3.1. Reconstruction of the froth surface height

To demonstrate the proposed method, froth overflowing the cell lip was analyzed over a duration of 4 s, corresponding to a sequence of 200 frames. Figure 2a shows the camera 1 image of the froth surface at $t_1 = 2$ s (i.e., the 100th frame), along with the chosen region of interest (ROI). Two distinct froth features are visible in this image: a large froth bubble located at the launder, and a region at the top right of the ROI where no froth is visible.

Applying the 3D froth surface reconstruction method to the image pair captured at t_1 yields the reconstructed froth surface shape shown in Figure 2b. The Z axis represents the froth surface height above the bottom of the cell, as illustrated in Figure 1a. The 3D reconstruction accurately resolves both the large bubble at the launder ($X = 70$ mm, $Y = 15$ mm), and the froth-free zone in the upper-right region of the launder ($X = 120$ mm, $Y = 30$ mm), aligning closely with visual observations from the 2D image (Figure 2a). The elevated height at the edges of the ROI ($X = 0$ mm and $X = 150$ mm) can be attributed to froth adhering to the sidewall of the cell. Additionally, an elevated froth agglomerate is visible near the lower boundary of the ROI ($X = 60$ mm, $Y = -30$ mm).

Figure 2c shows the froth height averaged over the 4 s measurement period, projected onto the XY plane. The average height remains elevated at the locations of the big bubble and the froth agglomerate, and is reduced at the froth-free launder region. The presence of these distinct froth features in the averaged image indicates that the froth structure underwent only little displacement during the short measurement period.

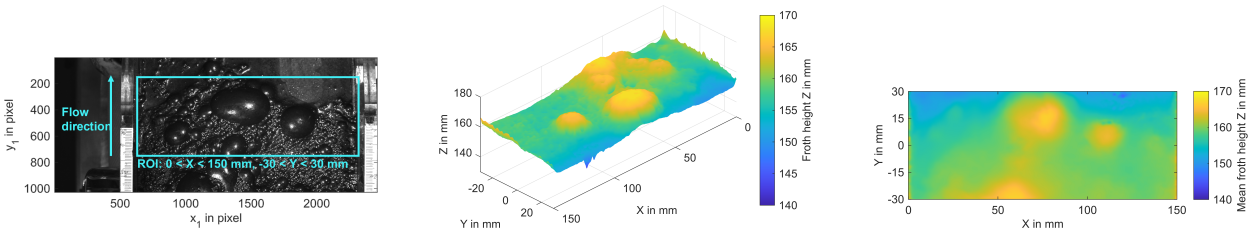

(a) Raw image from camera 1 at $t_1 = 2$ s, with the ROI marked in blue.

(b) Instantaneous 3D reconstruction of the froth surface at t_1.

(c) Time-averaged froth surface height.

Figure 2: 3D reconstruction of an overflowing froth over a 4 s measurement period.

3.2. Overflowing froth height profiles

Now, another period of the experiment is analyzed where the froth is overflowing the cell lip. From the 3D reconstruction, height profiles of the overflowing froth in Y direction were extracted to characterize the froth flow

behavior at the lip. Two representative examples are presented to illustrate how the height profile shape correlates with differences in froth stability and mobility.

The first example shown in Figure 3 presents a wet, fast flowing froth. Figure 3a shows the froth height averaged over a 1.5 s measurement period. As in previous observations, the froth height is significantly reduced in the top-right corner of the reconstructed surface ($X = 120$ mm, $Y = 30$ mm) which is linked to a froth-free region on the launder. On the reconstructed surface, two ROIs of 20 mm width and 80 mm height were defined: ROI 1, located in a region of consistent overflow, and ROI 2, positioned at the froth-free launder region.

Figure 3b presents the froth height profiles in Y direction for the two ROIs, averaged across the X coordinates. The figure shows both the time-averaged froth height profile over the entire measurement period, and five instantaneous profiles extracted from individual image pairs. Both time-averaged profiles have a nearly horizontal froth surface within the flotation cell (-40 mm $< Y <$ 15 mm), followed by a gradual decline in froth height over the tilted launder (15 mm $< Y <$ 40 mm). For $X <$ 15 mm, the froth height profiles are nearly identical, indicating similar froth behavior on both sides of the flotation cell. Notably, the profile for ROI 2 reveals a reduction in froth height at $Y \gtrapprox 15$ mm, which corresponds to the froth-free launder region. This example demonstrates the capability of the 3D reconstruction method to detect localized absence of froth overflow at specific points along the cell lip.

As a second example, Figure 4 shows a difference in froth overflow between the two ROIs: no froth is observed flowing over the right side of the launder (ROI 2), while the left side reveals elevated froth levels (ROI 1). The time-averaged height profiles directly reflect this difference. In ROI 1, the froth is is elevated much higher within the flotation cell ($Y < 0$ mm), generating sufficient potential energy to overflow the cell lip. In contrast, ROI 2 shows much lower froth heights within the flotation cell, hindering the overflow. The inhomogeneous froth height in the flotation cell may result from the direction of rotor rotation, which is transmitted to the froth phase.

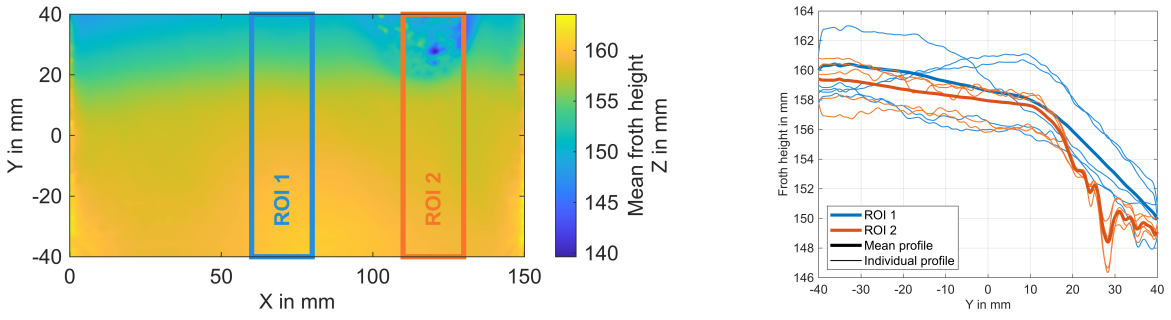

(a) Froth surface height averaged over measurement period.

(b) Froth height profiles.

Figure 3: Height profiles of a wet, fast-flowing froth overflowing the lip of a flotation cell (at $Y = 0$), averaged over a 1.5 s measurement period, for two regions of interest (ROIs). ROI 1 covers a region of consistent froth overflow, while the launder is froth-free in ROI 2 for $Y > 20$ mm.

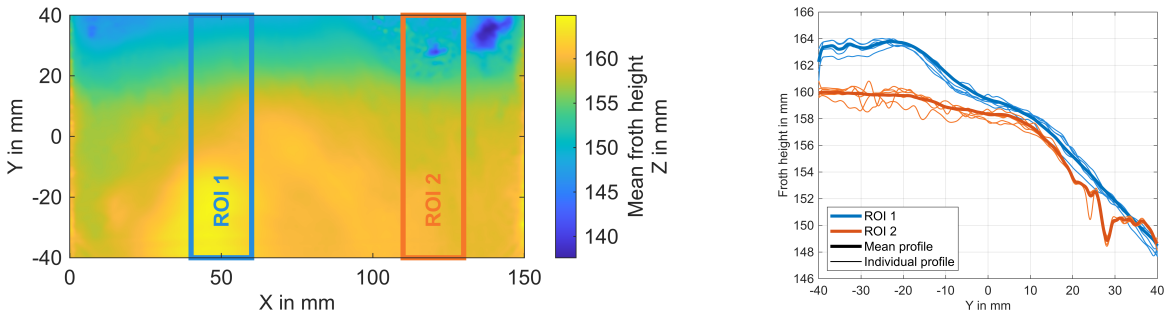

(a) Froth surface height averaged over measurement period.

(b) Froth height profiles.

Figure 4: Height profiles of a wet, fast-flowing froth overflowing the lip of a flotation cell (at $Y = 0$), averaged over a 0.5 s measurement period, for two regions of interest (ROIs). Elevated froth levels in the cell and on the launder in ROI 1, while no froth is overflowing in ROI 2.

4. Discussion

4.1. Froth stability

In addition to analyzing froth height profiles, the method could also be applied for measuring froth stability. Since froth stability is directly related to the bubble burst rate, imaging-based measurement techniques typically detect bubble ruptures by identifying changes between consecutive 2D images (Morar et al., 2012). However, these approaches require bubble segmentation, and their accuracy depends on the quality of the segmentation. The segmentation algorithm has to be tailored to the specific froth appearance in a given process, and can be influenced by variations in lighting or the distance between the froth surface and the camera.

While the bursting of froth bubbles can be observed in 2D images, it is also linked to sudden local reduction in froth layer thickness. Thus, 3D measurements can overcome the limitations of 2D approaches by integrating froth depth information into stability analysis. Liu et al. (2022) used a Microsoft Kinect sensor to incorporate froth depth information into bubble burst detection. However, this method still requires bubble segmentation at the froth surface. A more precise 3D measurement of froth bubble depth would eliminate the need for bubble segmentation, instead using the fluctuation of froth surface height as an indicator of froth stability. Unstable froths, where bubbles are bursting frequently, would show a much higher fluctuation than stable froths.

This relation is demonstrated through two representative examples. Figure 5 presents a sequence of three consecutive frames captured at 50 frames per second showing the bursting of a large bubble. Figure 5a shows the intact bubble before the rupture, and Figure 5b, shows the moment of rupture. In Figure 5c, the bubble has fully burst, exposing the finer bubbles underneath. This event is reflected in a significant reduction in the corresponding froth surface height at the location of the former bubble. Before the bubble burst, the froth height at $X = 45\,\text{mm}, Y = 5\,\text{mm}$ was approximately 167 mm above the bottom of the flotation cell (Figure 5d). After the burst, the froth height in this location has reduced by 13 mm to 154 mm (Figure 5f). In contrast, the surface height of the more stable froth shown in Figure 6 remains nearly constant during the three consecutive images, indicating no collapse of large froth agglomerates.

This examples illustrate how the 3D reconstruction could be used to quantify the stability of overflowing froth, for

example by computing the cross-correlation between subsequent reconstructed 3D surface shapes. Here, it is essential to correct for the displacement of the froth bulk caused by the froth bubble motion towards the weir (Zhang et al., 2020). The displacement depends on froth velocity and imaging frame rate and would distort cross-correlation results otherwise.

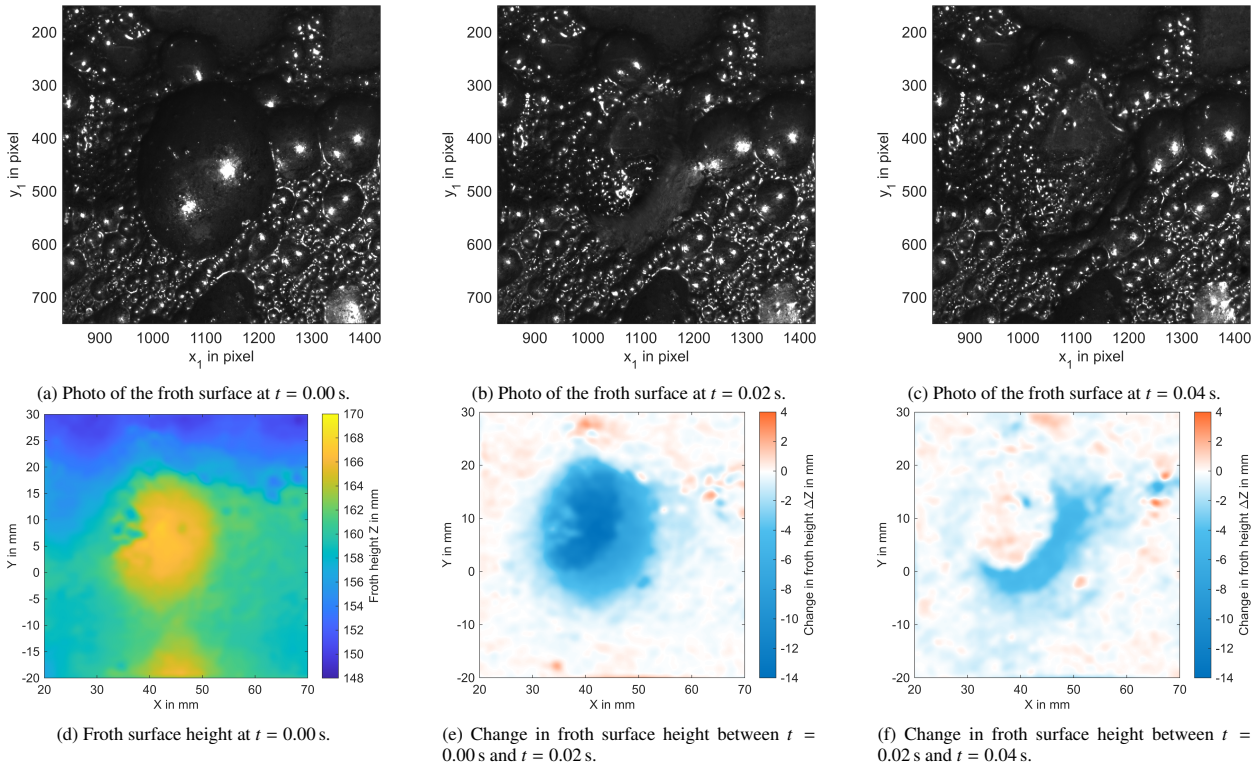

(a) Photo of the froth surface at $t = 0.00$ s.

(b) Photo of the froth surface at $t = 0.02$ s.

(c) Photo of the froth surface at $t = 0.04$ s.

(d) Froth surface height at $t = 0.00$ s.

(e) Change in froth surface height between $t = 0.00$ s and $t = 0.02$ s.

(f) Change in froth surface height between $t = 0.02$ s and $t = 0.04$ s.

Figure 5: Detection of a large bursting bubble in the 3D reconstructed froth surface. At $t = 0.00$ s, the bubble is fully intact, at $t = 0.02$ s, it is rupturing, and at $t = 0.04$ s, it has fully collapsed. Figures 5e and 5f show that the bursting event is reflected in a sudden decrease of the measured froth surface height.

4.2. Sources of uncertainty in the 3D reconstruction of the froth surface

The 3D froth reconstruction method proved effective for extracting and analyzing height profiles of overflowing froth. The method accurately resolves details of the froth surface, including larger individual bubbles, enabling the detection of bubble bursts as a basis for the assessment of froth stability.

The photogrammetry approach presented here is based on image disparities. This is particularly suitable for froth imaging as it drastically reduces the search space for corresponding points and thus improves computational efficiency. However, due to the necessary image rectification, this method strongly relies on the accurate positioning and calibration of the cameras as well as suitable illumination. The position and settings of the cameras directly influence the accuracy of the 3D reconstruction and must be carefully optimized depending on the froth characteristics and imaging system capabilities. The aim is to acquire evenly illuminated, high-contrast, and sharply focused images that fully cover the desired field of view. Regarding camera positioning and field of view, the distance between the

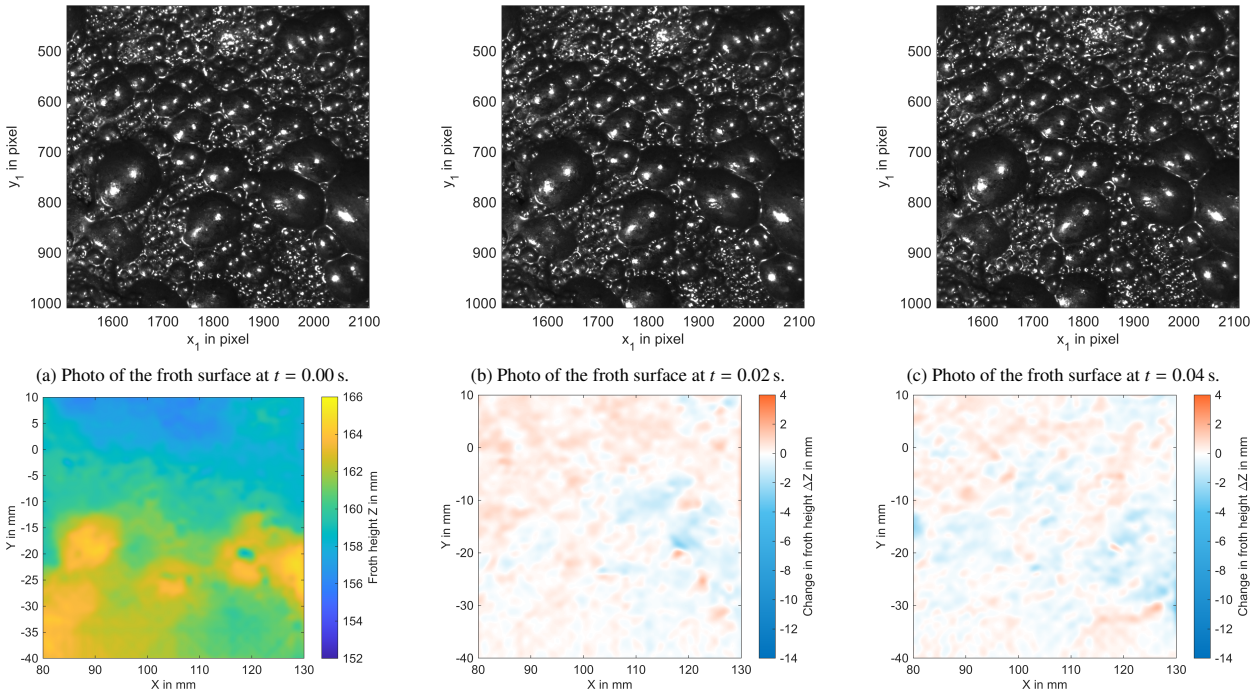

(a) Photo of the froth surface at $t = 0.00$ s.

(b) Photo of the froth surface at $t = 0.02$ s.

(c) Photo of the froth surface at $t = 0.04$ s.

(d) Froth surface height at $t = 0.00$ s.

(e) Change in froth surface height between $t = 0.00$ s and $t = 0.02$ s.

(f) Change in froth surface height between $t = 0.02$ s and $t = 0.04$ s.

Figure 6: Stable froth with a low fluctuation of the froth surface height. The three consecutive photos show only minor changes in the froth surface, which reflects in only minor changes of the measured froth surface height.

cameras and their distance to the froth surface determine the field of view, which affects the disparity range and thus the accuracy of the 3D reconstruction, particularly the uncertainty in the Z coordinate measurement. In terms of illumination and sharpness, a small aperture increases the depth of field, which is essential for maintaining sharp focus across the range of froth surface heights. However, this requires longer exposure times to maintain adequate image brightness, consequently increasing motion blur.

5. Conclusion

In this study, we present stereo photogrammetry for measuring the surface of froth overflowing the lip of a flotation cell. Unlike conventional froth imaging methods that rely on 2D imaging, our approach enables full 3D surface reconstruction of the froth using two calibrated stereo cameras and calculating disparity maps from rectified image pairs. We have demonstrated a proof-of-concept of the proposed method in a laboratory-scale flotation cell. The method accurately resolves the froth surface shape including large bubbles, their movement and rupture. The extracted height profiles allow to distinguish between areas with or without froth overflowing the cell lip, and allow to derive information on froth stability and froth mobility at the cell lip. Beyond the study of height profiles in flow direction, the method could also significantly improve the accuracy of air recovery measurements by enabling spatially resolved measurement of froth height and velocity.

Acknowledgements

The financial support of the German Helmholtz Association within the frame of the project "Securing raw materials supply through flexible and sustainable closure of material cycles" is gratefully acknowledged. The authors thank Peggy Jähnigen (Institute of Fluid Dynamics, Helmholtz-Zentrum Dresden-Rossendorf) for assistance in planning and conducting the laboratory flotation experiments.

References

Aldrich, C., Avelar, E., Liu, X., 2022. Recent advances in flotation froth image analysis. Minerals Engineering 188, 107823. doi:10.1016/j.mineng.2022.107823.

Aldrich, C., Marais, C., Shean, B., Cilliers, J., 2010. Online monitoring and control of froth flotation systems with machine vision: A review. International Journal of Mineral Processing 96, 1–13. doi:10.1016/j.minpro.2010.04.005.

Hadler, K., Cilliers, J., 2009. The relationship between the peak in air recovery and flotation bank performance. Minerals Engineering 22, 451–455. doi:10.1016/j.mineng.2008.12.004.

Hirschmüller, H., 2005. Accurate and Efficient Stereo Processing by Semi-Global Matching and Mutual Information, in: 2005 IEEE Computer Society Conference on Computer Vision and Pattern Recognition (CVPR'05), IEEE, San Diego, CA, USA. pp. 807–814. doi:10.1109/cvpr.2005.56.

Hu, F., Fan, Y., Ma, X., Dong, X., Feng, Z., Sun, Y., Niu, J., 2024. 3D feature characterization of flotation froth based on a dual-attention encoding volume stereo matching model and binocular stereo vision extraction. Minerals Engineering 217, 108903. doi:10.1016/j.mineng.2024.108903.

Liu, L., Zhou, X., Liao, Q., Hu, W., Zhao, L., 2022. Burst bubble recognition based on depth feature, in: Yang, Z., Xing, Y., Zhou, Y., Wu, L., Chen, Z. (Eds.), 4th International Conference on Informatics Engineering & Information Science (ICIEIS2021), SPIE. p. 72. doi:10.1117/12.2627429.

Luhmann, T., Robson, S., Kyle, S., Boehm, J., 2020. Close-Range Photogrammetry and 3D Imaging. De Gruyter, Berlin, Boston. doi:10.1515/9783110607253.

Luo, J., Tang, Z., Zhang, H., Fan, Y., Xie, Y., Gui, W., 2023. A binocular camera calibration method in froth flotation based on key frame sequences and weighted normalized tilt difference. IEEE Transactions on Circuits and Systems for Video Technology 33, 5576–5586. doi:10.1109/TCSVT.2023.3260901.

Marquardt, T., Hassan, A., Jähnigen, P., Lappan, T., Pereira, L., Heitkam, S., Rudolph, M., , Eckert, K., 2025a. Optical measurement of froth height and depth in a batch flotation test. Submitted to Measurement Science and Technology.

Marquardt, T., Naumann, P., Lappan, T., Sommer, A.E., Eckert, K., Heitkam, S., 2024. Laser-based methods for foam and froth height measurement, in: Rauh, C., Ruck, B., Leder, A. (Eds.), Proceedings of the 31. Fachtagung "Experimentelle Strömungsmechanik", German Association for Laser Anemometry GALA e.V., Karlsruhe. URL: `https://www.gala-ev.org/images/Beitraege/Beitraege2024/pdf/05.pdf`.

Marquardt, T., Naumann, P., Lappan, T., Ziauddin, M., Sommer, A.E., Eckert, K., Heitkam, S., 2025b. Laser-based measurement of overflowing foam height profiles. Poster presented at the Jahrestagung DECHEMA/VDI-Fachgruppen Mischvorgänge, Hochdruckverfahrenstechnik und Mehrphasenströmungen, March 19–21 2025, Hamburg, Germany.

Mesa, D., Brito-Parada, P.R., 2019. Scale-up in froth flotation: A state-of-the-art review. Separation and Purification Technology 210, 950–962. doi:10.1016/j.seppur.2018.08.076.

Morar, S.H., Bradshaw, D.J., Harris, M.C., 2012. The use of the froth surface lamellae burst rate as a flotation froth stability measurement. Minerals Engineering 36-38, 152–159. doi:10.1016/j.mineng.2012.03.018.

The MathWorks, Inc., 2025a. disparitySGM: Compute disparity map through semi-global matching. URL: `https://de.mathworks.com/help/vision/ref/disparitysgm.html`. Accessed: 2025-07-22.

The MathWorks, Inc., 2025b. scatteredInterpolant: Interpolate 2-D or 3-D scattered data. URL: `https://de.mathworks.com/help/matlab/ref/scatteredinterpolant.html`. Accessed: 2025-09-18.

Zhang, H., Tang, Z., Xie, Y., Gao, X., Chen, Q., Gui, W., 2020. A Similarity-Based Burst Bubble Recognition Using Weighted Normalized Cross Correlation and Chamfer Distance. IEEE Transactions on Industrial Informatics 16, 4077–4089. doi:10.1109/TII.2019.2960051.

Zhao, L., Peng, T., Xie, Y., Gui, W., Zhao, Y., 2019. Froth Stereo Visual Feature Extraction for the Industrial Flotation Process. Industrial & Engineering Chemistry Research 58, 14510–14519. doi:10.1021/acs.iecr.9b00426.

Zheng, X., Li, X., Yuan, Z., Ban, X., 2024. Visual measurement of foam thickness in flotation process based on depth stereo matching, in: 2024 International Conference on Automation in Manufacturing, Transportation and Logistics (ICaMaL), pp. 1–9. doi:10.1109/ICaMaL62577.2024.10919521.

Zhong, Y., Tang, Z., Zhang, H., Xie, Y., Dai, Z., 2024. Measurement of froth-layer depth with binocular camera based on intensity correction and its application to pulp-grade monitoring. IEEE Transactions on Instrumentation and Measurement 73, 1–9. doi:10.1109/TIM.2024.3420351.